Scattering and absorption in 2D optics

Mariani, F.

Chapter 5

Light propagation in rough thin-film solar cells

We investigate scattering and propagation of light in rough thin-film Silicon solar cells, a quasi two dimensional absorbing random scattering medium. We use various techniques where we image the cell under structured coherent illumination with both intensity and phase-step function, or measure the angular distribution of the scattered light. By combining these measurements with polarization selection, and comparing them with a reference sample, we study the depolarization properties of the solar cell and obtain information on the transport and absorption of light in our sample. We model the results in terms of the guided modes of the structure and of the reflection at the skewed surfaces of the rough structure. Understanding light transport and photon management is a step towards the improvement of the performances of solar cells.

5.1 Introduction

In the quest for clean sources of energy, photovoltaic technologies play a prominent role and much research effort is thus devoted to optimize the performance of solar cells. Improvements can involve various aspects: the production process, the absorbing material, the structure of the cell [1], and the light collection and trapping strategy [2, 3, 4]. Of all the possible forms of photovoltaic devices, thin-film silicon single-junction solar cells are the simplest and most widespread, for the simplicity of their structure and the modest cost of production.

The performance of a thin-film solar cell depends on many parameters, the thickness being one of them. The thickness affects both the probability for light to generate charge carriers, and the efficiency of carriers collection at the electrodes. For instance in nano-crystalline silicon (nc-Si), the absorption length for light with $\lambda = 633$ nm is 2.5 μm: a much thinner layer of Si gives a reduced optical path in the absorbing medium for light at this wavelength, and thus fewer charge carriers generated. On the other hand, a thinner absorber reduces the losses during charge transport to the electrodes of the cell, allowing a more efficient collection of the photovoltaic current. A compromise between these two aspects leads, for single junction cells, to a typical thickness of the order of 1-10 μm, also varying on the type of Si used.

One way to increase the coupling of light to a semiconductor device is to introduce scattering, e.g. by employing patterned interfaces [5, 6, 7]. Compared to a flat interface, a structured one scatters light at high angles inside the solar cell, also beyond the angle of total internal reflection. This effectively traps the light and allows to achieve higher external efficiency in cells with a thickness smaller than the typical absorption length.

Several patterning strategies can be used: plasmonic particles [3], periodic dielectric structures [8, 9] or optimized random patterns [10, 11]. The latter offer the advantage of having a truly broad spectral response [12]; also, these can be relatively easily fabricated, for instance by chemically etching the substrate. For some configurations the increase in light absorption can be up to one order of magnitude relative to similar flat structures [13], and beat conventional limits for absorption enhancement [2].

Randomly patterned thin solar cells are quasi-2D random scattering medium. Extensive research already exists for the control of light in truly three dimensional random scattering media [14]. In that case it was demon-

strated that light propagation can be controlled with the use of wavefront shaping techniques to achieve tight localization in a focus spot [15, 16], to image through a scattering medium [17], and to maximize the amount of fluorescence generated by a weakly absorbing medium [18]. These techniques rely on the linear properties of the scattering process and the transmission matrix [19] and have not yet been applied to quasi-2D samples involving scattering thin layers, in particular in the presence of absorption. This raises the question of to what extent wavefront shaping techniques can be used to enhance absorption also in very thin textured silicon solar cells.

The concept of achieving high absorption in 3D random scattering media was theoretically and numerically explored by Chong et al. [20] and named Coherent Enhanced Absorption (CEA). The increase of absorption is theoretically possible in random media in a broad range of wavelengths [20]. A first attempt of the use of wavefront shaping in an organic solar cell has shown the possibility to localize the light absorption near the electrodes of the cell to reduce the electron transport losses and thus increase the cell external quantum efficiency [21]. Nevertheless, CEA is physically different from an optimization of the carrier collection, so its potential in thin-Si solar cells remains to be demonstrated.

The possibility of using wavefront shaping to control the light distribution in random media requires light to propagate in the medium and produce interference phenomena, which can be advantageously exploited. In this work we investigate light transport within a solar cell, in order to quantify the potential for CEA in single thin nano-crystalline silicon (nc-Si) textured cells. In particular, we investigate which fraction of the incident field penetrates inside the Si layer, escapes from the cell, and is scattered back outside.

We perform our experiments using coherent illumination and studying the backscattering properties of the sample. Depolarization properties of the solar cell play an important role in our study; despite being a minor effect with little relevance for studies of electronic performances, they provide additional insight on the scattering and transport mechanisms. Moreover, by looking at depolarized light we are able to minimize the effect of stray-light in our measurements.

After introducing in Sec. 5.2 and 5.3 the sample we use and the experimental setup, we present in Sec. 5.4 our studies of polarization-resolved reflection, identifying both the positions from where reflected light originates and its angular properties. Further, we investigate the transport properties of the

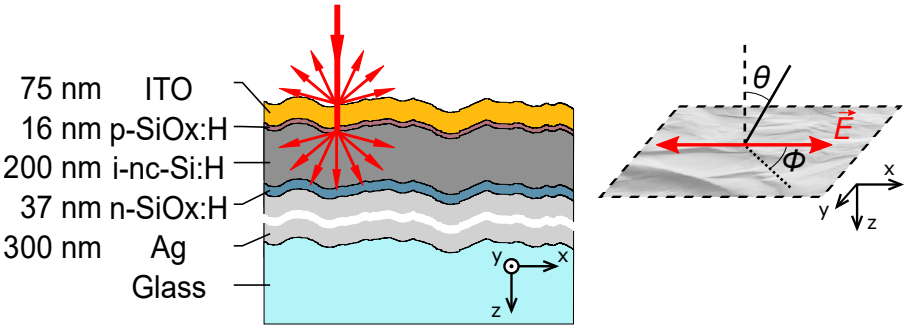

Figure 5.1: Left: a cross section of the rough thin-film solar cell used in the experiments including the nominal thickness of each layer. The roughness of the cell is defined by the glass substrate, on top of which the other layers are deposited. The roughness depth and profile are on scale, and extracted from AFM measurements. The relative thickness of all layers is also on scale. Right: definition of the polar angles used in the remainder of the text, defined with respect to the normal to the average sample plane (dashed line) and to the direction of the incident polarization (electric field in red)

layered structure by using knife-edge illumination and report the results in Sec. 5.6. In Sec. 5.7 we model the light-guiding properties of our structure. A general discussion on the results is given in Sec. 5.9.

5.2 Thin-film Si solar cell

The solar cell used in our experiment was fabricated in the department of Electrical Sustainable Energy, led by Prof. M. Zeman at the Technical University of Delft. A scheme of the solar cell is shown in Fig. 5.1. This cell is composed of several layers deposited on a nano-patterned glass substrate, located at the back of the cell. The glass surface defines the roughness of the cell as each layer reproduces the morphology of the underlying one. The first material deposited on the glass substrate is a 300 nm thick Silver layer. This serves two purposes: it reflects the incoming radiation back into the layers above, thereby doubling its optical path in the absorbing material, and it acts as back contact. The presence of the Ag reflector makes it impossible to perform transmission measurements on our solar cell. The absorptive layers are evaporated on top of the Ag reflector in the form of a three-layer p-i-n structure, with nominal thickness of 16 nm (p-SiOx:H), 200 nm (i-nc-Si:H) and 37 nm (n-SiOx:H). A 75 nm layer of transparent conductive tin oxide (ITO) is deposited as a front contact for the cell.

Our sample is similar to commercially available solar cells but much thin-

ner; this does not maximize the generation of photo current but simplifies the study of light transport by reducing the number of allowed guided modes propagating in the solar cell. Figure 5.2 shows part of the morphology of our solar cell with the roughness characterized by atomic force microscopy (AFM). From the topographic profile we can determine the root mean square (rms) roughness σ_{rms} and its lateral correlation length l_c. For our sample we obtain $\sigma_{rms} = 165$ nm and $l_c \simeq 1.2$ μm.

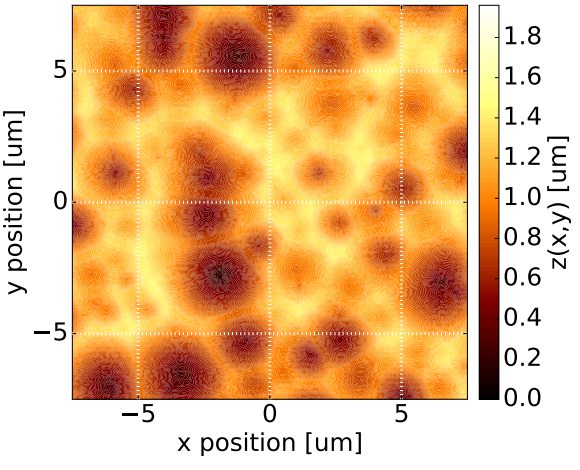

Figure 5.2: AFM profile of a portion of the surface of the solar cell used in our study shows that the structure is organized in *valleys* and ridges with average size of $l_c \simeq 1.2$ μm.

5.3 Experimental Setup

We study the scattering properties of our solar cell with the backscattering microscope setup depicted in Fig. 5.3. Light from a He-Ne laser ($\lambda = 632.8$ nm) is routed through a single-mode fiber and collimated in a Gaussian beam of diameter 3.3 mm; its polarization is set horizontal with the polarizer P_0. The beam is reflected by a phase-only reflective spatial light modulator (SLM) which is imaged on the sample surface using a telescope composed of a tube lens L_1 ($f = 200$ mm) and a microscope objective (100x, NA $= 0.9$). Possible spurious depolarization effects from the SLM are removed with an additional polarizer P_1. The polarization of the light incident on the sample is oriented along x. In front of the SLM we mount a knife edge that can be moved in the beam to obscure half of it.

The light reflected from the solar cell is collected through the same objective and imaged on a CCD camera after passing through a second tube lens L_2

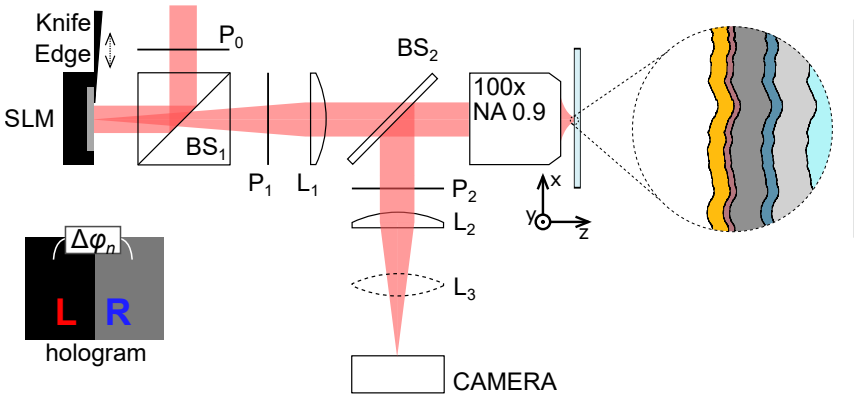

Figure 5.3: The experimental setup: a collimated laser beam illuminates the spatial light modulator (SLM) after passing through polarizer P_0. The light reflected by the SLM is polarized again with polarizer P_1 and imaged on the sample with microscope optics comprising of a tube lens L_1 (f = 20 cm) and a 100x microscope objective (NA=0.9). The reflected light is collected with the same objective. The sample is imaged with a second tube lens L_2 (f = 20 cm) on a CCD camera, after passing through the analyser P_2 which selects the polarization of the detected light. In the encircled inset a magnified view of the rough solar cell. The bottom left inset shows a scheme of the hologram projected on the SLM for the phase-step method.

($f = 200$ mm). The analyser P_2, mounted on a computer controlled rotating stage, selects the linear polarization of the reflected light to be either parallel or orthogonal to the incident polarization. Our setup also employs a flip-lens L_3 ($f = 100$ mm) which allows to obtain information on the far field of the light reflected by the sample.

The sample is mounted on a 3-axis piezo-stage for precise positioning. We correct our data for the polarization dependent reflectance of the beam-splitter BS_2 and for the incident intensity, adjusted using neutral density filters (not shown in Fig. 5.3) to use the full dynamic range of our camera in the different measurement configurations.

Although the wavelength we use falls within the band of the anti-reflection coating of the optics, residual interfacial reflection are the most prominent nuisance in our setup. These originate in particular from the microscope objective and affect the signal for measurements where P_2 is set to detect the polarization parallel to the incident one. A small shift of the objective off the optical axis reduces this unwanted intensity component by almost factor 10, although still leaving unwanted residuals (see Appendix 5.B). Also for this rea-

son we focus our analysis on the depolarized component of the backscattered light.

5.4 Polarization resolved reflection

Incident light interacts with the solar cell in a complex way and the reflected field carries information on the scattering occurring within the layered structure. We report the results on the overall reflectivity of our solar cell, on the position dependence of the reflected light on the sample surface, and on the angular distribution of the backscattered light. In particular, we look at the depolarization properties of the solar cell.

We use the setup shown in Fig. 5.3 without the knife edge. A flat bulk silicon wafer serves as a reference sample to measure the response of the instrument, and provides a comparison with the solar cell. This also allows a relative intensity calibration, by assuming the reflectance of silicon to be $\mathrm{R} = |r_{Si}|^2 = 0.347$, with r_{Si} the Fresnel coefficient for $\lambda = 0.633\,\mu$m for normal incidence. With the value for R we determine the signal expected at the camera for the incident intensity $I_{in}(x, y)$.

5.4.1 Total reflectance measurements

We first determine the total reflection from both the reference sample and the solar cell. The light backscattered from the solar cell has a speckle-like structure with a Gaussian envelope; we average the data recorded at ten different positions on the sample surface to obtain a smoother ensemble-averaged profile $\bar{I}_{\parallel/\perp}(x, y)$

We first examine the results for the Si reference sample. While for the parallel polarization we have $\bar{I}_{\parallel}/\bar{I}_{in} = 0.347$ by definition, for the orthogonal polarization we measure $\bar{I}_{\perp}/\bar{I}_{in} = 5.5 \cdot 10^{-5}$. We define the depolarization ρ as the ratio between the total intensity reflected in the orthogonal polarization with respect to the one in parallel polarization. For the reference sample we find $\rho = I_{\perp}/I_{\parallel} \simeq 1/6500$. This result is comparable to the extinction ratio specified for the analyser P_2 (1:10000) and suggests that $\bar{I}_{\perp}(x)$ for the reference sample is the remaining of the specularly reflected light.

The solar cell reflectance is measured with the same approach. The cell yields $\bar{I}_{\parallel}(x)/\bar{I}_{in}(x) = 0.43$ in parallel polarization and $\bar{I}_{\perp}(x)/\bar{I}_{in}(x) = 8.9 \cdot 10^{-3}$ for the orthogonal polarization, giving a depolarization ratio $\rho = I_{\perp}/I_{\parallel} = 1/48$.

For parallel polarization the solar cell reflects more than the silicon by a factor 1.24 (see Fig. 5.9). We attribute this to the presence of the Ag back-reflector. More important, our sample shows a much stronger signal for light backscattered in the orthogonal polarization (200 times more than the reference), indicating that scattering by surface texturing plays a role in depolarization properties of our structure.

We note that the higher reflectance values for the rough solar cell are underestimations of the real values, because the light collection is limited by the numerical aperture of the setup.

Despite a clear depolarization effect, the solar cell reflection with $\rho \simeq 0.02$ is still surprisingly polarized as compared, for instance, to a volume scatterer such as white paint, for which $\rho \simeq 0.89$ (see Ch. 4). Although relatively weak, depolarized light is interesting because it has potentially undergone multiple scattering events. We examine this polarization component more closely.

5.4.2 Polarized imaging

We investigate depolarization happening at the solar cell by imaging the reflected intensity in parallel polarization $I_{\parallel}(x, y)$, as well as the intensity $I_{\perp}(x, y)$ reflected at orthogonal polarization. The results are shown in Fig. 5.4 for a small region of the sample, in a single position. To highlight the effect of coherence in the backscattering of the cell, we also show an image of the solar cell under incoherent illumination, obtained by illuminating the sample with light from a halogen lamp, filtered in the spectral band $625 \pm 15\,\mathrm{nm}$ to avoid chromatic aberrations.

In the case of reflection from coherent illumination detected in parallel polarization, shown in Fig. 5.4 (a), light is mainly organized in ring-like structures which are reminiscence of the rims and valleys of the roughness topology shown in Fig. 5.2. This intensity distribution is accompanied by concentric rings towards the center of the valleys, which is also frequently a bright spot.

For orthogonal polarization, shown in Fig. 5.4 (b), the distribution of the intensity appears to be complementary to the one observed under parallel polarization: it is mostly localized in spots that hardly scatter in parallel polarization and hence is also correlated with the morphology.

The patterns in Fig. 5.4 are not a novelty: reflected intensity distribution similar to the one we measure have also been observed in transmission on rough ZnO interfaces [22, 23, 24]. In this case, bright rim-like structures were measured with near-field techniques. These were attributed to guided modes

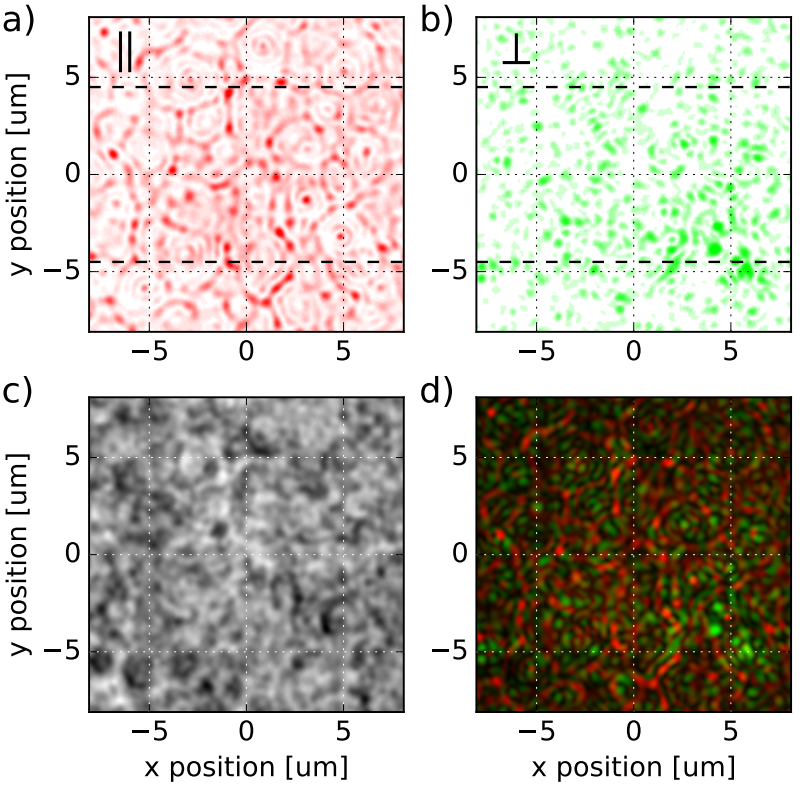

Figure 5.4: Images of the surface of the solar cell under different conditions: a,b) coherent illumination with horizontally polarized laser light (633 nm), observed for polarization respectively parallel (a) and perpendicular (b) to the incident one; c) incoherent illumination from spectrally filtered halogen lamp (625 ± 15 nm), where bright areas correspond to locations with higher reflectivity; d) overlay of panels a) and b) for direct comparison. The brightness of the two color scales are not proportional to the reflected intensities, which in orthogonal polarization is on average a factor 1/48 weaker than the intensity reflected in parallel polarization. The dashed lines in panels (a-b) indicate the strip considered in Sec. 5.6 for data averaging along y.

propagating in the structure and to standing waves which preferentially occupy the rims of the surface topology. The brighter areas were also identified as the spots of highest absorption enhancement with respect to an unstructured sample [23].

The similarity between our results and these earlier works is surprising for several reasons. First, for the measurement technique: the previous studies were based on near-field detection techniques, with access to the full angu-

lar spectrum of the emission, whereas our detection is necessarily limited by the numerical aperture of the objective. Secondly, for the sample structure: the ZnO layers were deposited on flat glass, rough only on the upper side, whereas our sample has a stratified structure. Finally the textured ZnO was illuminated through the substrate, whilst our reflection measurements include contributions from multiple surfaces, including the Ag reflector. The observed analogies indicate that the distribution of intensity in parallel polarization is partially determined by the topology of the sample.

We also calculate the intensity probability distribution $P_{\parallel/\perp}(I)$ for the intensity profiles $I_{\parallel/\perp}(x, y)$ shown in Fig. 5.4 (a-b). The calculated $P_{\parallel/\perp}(I)$ show an exponential dependence, characteristic of fully developed speckles, for both parallel and perpendicular polarization. Hence, the intensity statistics of our patterns resembles that of speckles despite the possibility of recognizing in the patterns a correlation to sample morphology.

5.5 Angular reflection properties

We obtain additional information on the scattering processes at the solar cell by studying the angular properties of the backscattered light. We collect the reflection far-field profiles by introducing the additional flip lens L_3 ($f = 100$ mm) between the tube lens L_2 and the camera. We measure the reflected intensity in both polarizations $I_{\parallel/\perp}(\theta, \phi)$, with θ and ϕ respectively the polar and azimuthal spherical coordinates (see Fig. 5.1).

In Fig. 5.5 we show $\bar{I}_{\parallel}(\theta, \phi)$ and $\bar{I}_{\perp}(\theta, \phi)$, the average far fields obtained from measurements over 10 different positions on the solar cell. A sample of white paint serves as a comparison and as control for the instrumental response: this is a volume scatterer reflecting nearly equal amount of power in both polarizations (see Ch. 4). The backscattered far fields of the white paint are almost uniform profiles with little differences between the two polarization. For the solar cell, instead, the far fields show far more structure.

The angular profile $\bar{I}_{\parallel}(\theta, \phi)$ depicted in Fig. 5.5 (a) contains two main features: a diffuse component spread over a wide angle, and a bright spot centered at polar angle $\theta = 0$. These components are expected in the reflectance of a textured solar cell [25]. The interfacial reflections from the optics show up as a minor contribution to the specular reflection.

Both the diffuse and specular components are visible in the cross section in Fig. 5.5 (e). The diffuse part, with a maximum at $\theta = 0$, monotonically

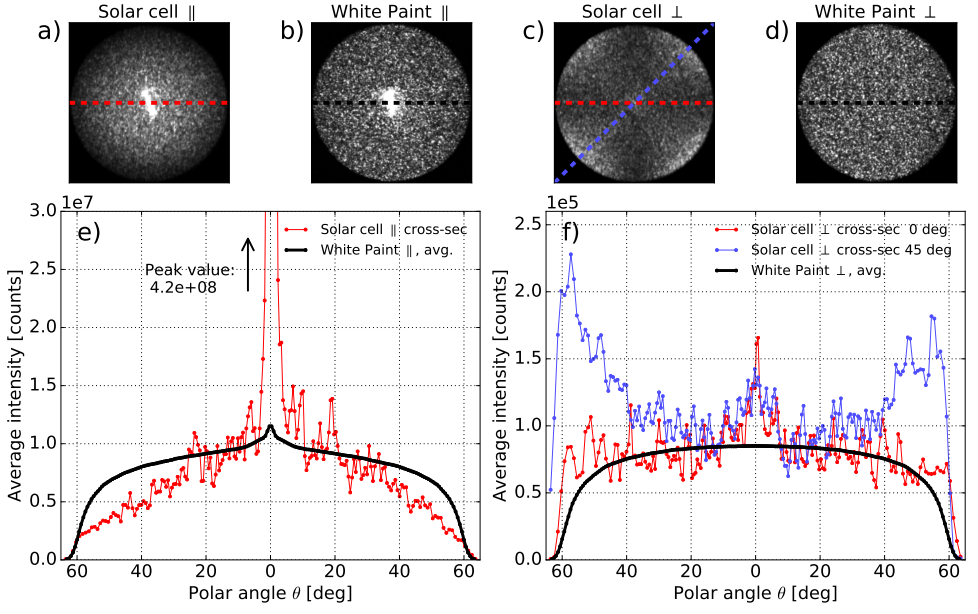

Figure 5.5: Far field reflection patterns from the solar cell and a sample of white paint, used as a comparison. Top panels (a-d): far field profiles for both parallel and orthogonal polarizations for the two samples. Bottom plots (e-f): reflected intensity profiles for parallel (left) and orthogonal (right) polarization. For the solar cell we report cross sections of the far field intensities (red and blue lines), obtained along the dashed lines in the upper panels, whilst for the white paint we show the azimuthally averaged profiles (black dashed line), conveniently rescaled for comparison purposes.

decreases with increasing polar angle and reduces to one fourth of its shoulder value at $\theta \simeq 60°$. The specular reflection instead has the form of a bright peak centred also at $\theta = 0$, with a full width half maximum of $1.2\,°$, which accounts for a fraction of 0.11 of the total collected reflected power. The attribution of this peak to the specular component is confirmed by the data for the flat-Si reference sample.

The depolarized component of the reflection $\bar{I}_\perp(\theta, \phi)$ is pictured in Fig. 5.5 (c). Differently from the parallel polarization case, this shows no specular peak and has a clear dependence on the azimuthally angle in the shape of four lobes peaked at the positions $\phi = (2n + 1)\pi/4$. The two cross sections of $\bar{I}_\perp(\theta, \phi)$ for $\phi = 0, \pi/4$, shown in Fig. 5.5 (f), help to see the relevance of the four peaks in the far field profile.

In order to understand the features of $\bar{I}_\perp(\theta, \phi)$ we write it as the sum of two components $I_C(\theta)$ and $I_A(\theta, \phi)$, the second describing the four-lobed

oscillation with ϕ:

$$I_{\perp}^{fit}(\theta,\phi) = I_A(\theta,\phi) + I_C(\theta,\phi) = A_{\perp}(\theta)\,\sin^2(2\phi) + C_{\perp}(\theta) \tag{5.1}$$

We use Eq. (5.1) to fit the measured far field $\bar{I}_{\perp}(\theta,\phi)$. In Fig. 5.6 (b) we show the calculated best values for the functions $C_{\perp}(\theta)$ and $A_{\perp}(\theta)$, together with the averaged profile for the diffuse reflection in parallel polarization $\left\langle \bar{I}_{\parallel}(\theta,\phi)\right\rangle_{\phi}$.

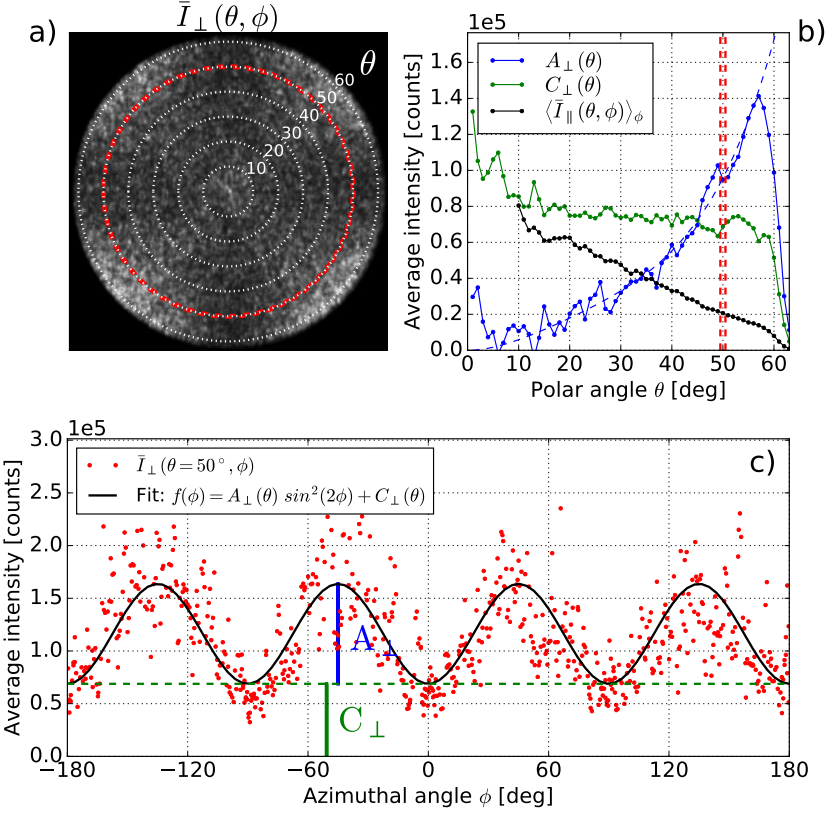

Figure 5.6: Analysis of the far field for the depolarized component of the solar cell reflection. (a) Average far field pattern $\bar{I}_{\perp}(\theta,\phi)$ with lines indicating constant polar angle values. The two red dashed circles highlight the region $\theta = (50 \pm 1)°$; (b) fit parameter $A_{\perp}(\theta)$ and $C_{\perp}(\theta)$ for the fit function from Eq. (5.1). The azimuthally average $\left\langle \bar{I}_{\parallel}(\theta,\phi)\right\rangle_{\phi}$ is shown, rescaled, for comparison. The red dashed lines indicate the region highlighted in a), while the dashed blue line is a 4^{th} order polynomial fit used later in the text. (c) Reflected intensity as function of azimuthal angle ϕ for the polar angle region $\theta = (50 \pm 1)°$ highlighted in a), with the best fit function.

The two functions $A_{\perp}(\theta)$ and $C_{\perp}(\theta)$ show no resemblance with each other

or with $\left\langle \bar{I}_{\parallel}(\theta,\phi) \right\rangle_{\phi}$. The coefficient $C_{\perp}(\theta)$ is almost constant in the accessible angular range, except for a peak located at $\theta < 10°$. The function $A_{\perp}(\theta)$, instead, tends to zero at $\theta = 0$ and increases continuously with θ, reaching a peak at the edge of the detection angle, with a value even two times higher than $C(\theta)$ at the same polar angle.

A possible origin for the four-lobed structure of $\bar{I}_{\perp}(\theta,\phi)$ is the polarization dependence of the Fresnel reflection coefficients. This explanation, detailed by the facets model in Appendix 5.A and formalized in Eqs. (5.13-5.14), captures both the $\sin^2(2\phi)$ dependence of the far field intensity as well as the shape of $A(\theta)$ profile, but not the presence of the azimuthally constant coefficient $C_{\perp}(\theta)$.

The facets model also predicts a weak two-lobed structure for the parallel polarization case. We check this in our data for $\bar{I}_{\parallel}(\theta,\phi)$ by fitting the measured far field with the model derived from Eqs. Eqs. (5.12) and (5.14):

$$I_{\parallel}^{fit}(\theta,\phi) = A_{\parallel}(\theta)\,\cos(2\phi) + C_{\parallel}(\theta) + \frac{A_{\parallel}^2(\theta)}{4\,C_{\parallel}(\theta)}\cos^2(2\phi) \tag{5.2}$$

The results of the fit, shown in Fig. 5.7, confirms that $\bar{I}_{\parallel}(\theta,\phi)$ oscillates twice along the azimuthal angle as predicted by the facets model. The values we find for $A_{\parallel}(\theta)$ and $C_{\parallel}(\theta)$ make the third term in Eq. (5.2) relatively small.

The results of this simple analysis for far fields patterns suggest that some of the features can be explained by a flat-interface reflection approximation applied to a rough interface. Nevertheless, we note that the ratio between the lobes amplitude and the constant signal for parallel polarization is $A_{\perp}(\theta)/\,C_{\parallel}(\theta) \simeq 0.03$ at $\theta = 50°$, while a similar calculation for a air-Si interface considered in appendix 5.A leads to a value about 10 times lower. We attribute the discrepancy between data and calculations to the simplification of the model, which doesn't account for the layered structure of the sample and thus neglects refraction and multiple scattering involving the Ag back-reflector.

The second contribution to the far field in orthogonal polarization is the diffuse component $I_C(\theta,\phi)$. This accounts for a fraction of the reflected power $P_C/(P_A + P_C) = 0.67$, with the optical powers calculated as $P_{A/C} = \int\int I_{A/C}(\theta,\phi)\,\theta\,d\theta d\phi$; this is equivalent to about 1% of the total power reflected by the solar cell. It is reasonable to assume that a far field component similar to $I_C(\theta,\phi)$ exists also for the reflection in parallel polarization,

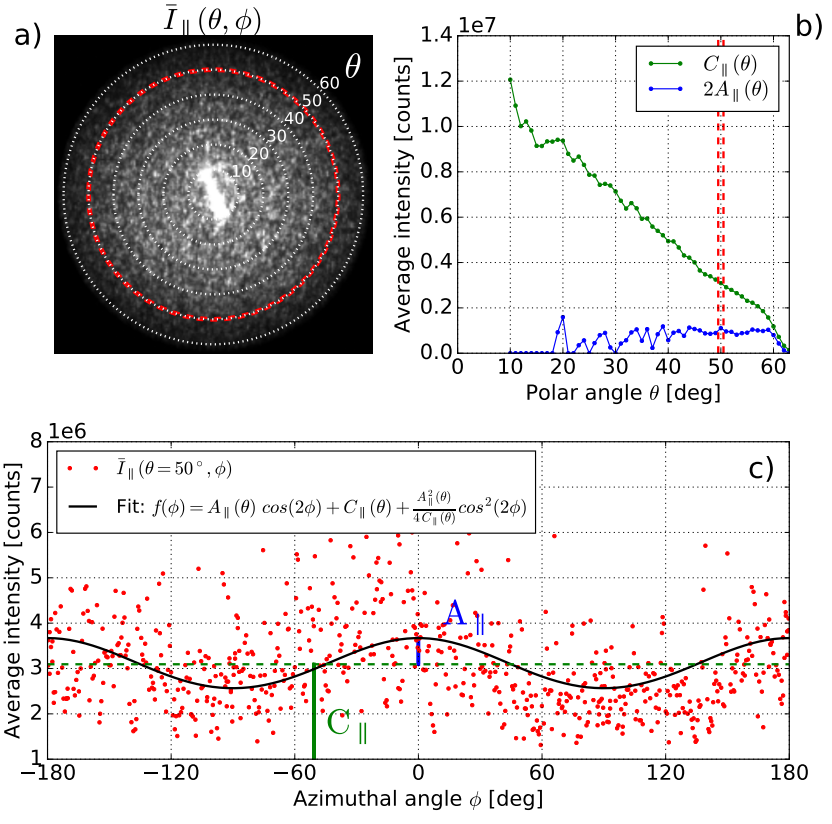

Figure 5.7: Cell reflection in parallel polarization, analysis of the far field. (a) average far field pattern $\bar{I}_{\perp}(\theta,\phi)$ with lines indicating constant polar angle values. The two red dashed circles highlight the region $\theta = (50 \pm 1)°$; (b) fit parameter $A_{\parallel}(\theta)$ and $C_{\parallel}(\theta)$ from the fit function in Eq. (5.2). The red dashed lines indicate the region highlighted in a). (c) reflected intensity as function of azimuthal angle ϕ for the polar angle region $\theta = (50 \pm 1)°$ highlighted in a), with the best fit function.

but this is not detectable as it would be much weaker than the much stronger diffuse signal (see Fig. 5.5 (e)).

It remains to specify the physical origin of $I_C(\theta,\phi)$. We attribute this to the fraction of the field, trapped in the waveguide-like structure, which escape from the solar cell after multiple scattering events. A confirmation for this interpretation comes from the shape of $I_C(\theta,\phi)$ which shows an additional peak centred at $\theta = 0$, which we attribute to coherent enhanced backscattering (EBS).

The origin of EBS is interference: this is a robust effect present in random scattering media [26, 27, 28], including rough interfaces, both metallic or

dielectric [29, 30]. In EBS reciprocal scattering paths interfere constructively and result in a peak centred at the backscattering direction with intensity up to two times the diffuse background. The backscattering cone can be obtained for both the co-polarized and depolarized light, with non-trivial differences between the two cases[31, 32, 33], and its width is Fourier related to the average propagation distance of the light in the scattering medium.

Figure 5.8 shows the details of the peak that we observe in $I_C(\theta)$. This is obtained by subtracting from $\bar{I}_\perp(\theta,\phi)$ the four-lobed component calculated as $\tilde{A}_\perp(\theta)\sin^2(2\phi)$, with $\tilde{A}_\perp(\theta)$ the 4^{th} order best fit polynomial for $A_\perp(\theta)$, obtained imposing $\tilde{A}_\perp(0)=0$ and $\tilde{A}'_\perp(0)=0$ and shown in Fig. 5.6.

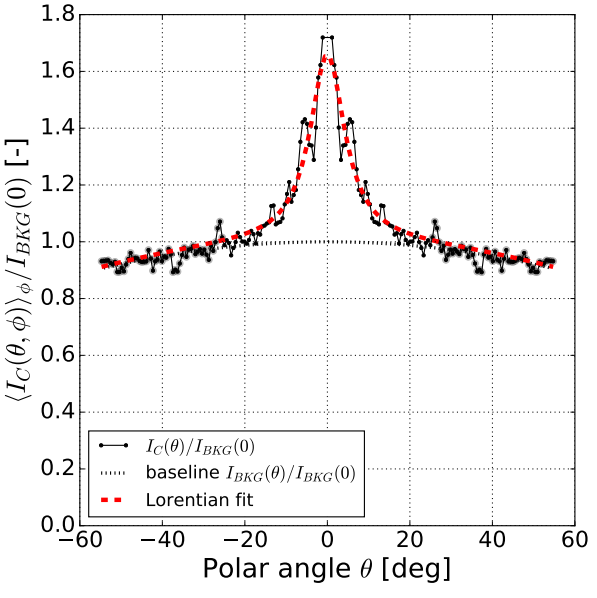

Figure 5.8: Result for the function $\langle I_C(\theta,\phi)\rangle_\phi$ calculated as explained in the text, highlighting the back scattering cone. Data are mirrored to negative θ to give a better impression of the peak. A 2^{nd} order polynomial is used to fit the background diffuse intensity $I_{BKG}(\theta)$ (dashed line). All intensities are divided by $I_{BKG}(0)$.

The exact shape of the enhanced backscattering peak requires a more detailed description; in absence of a theory for optical transport in our absorbing 2D scattering medium, we fit $I_C(\theta)$ with the sum of a phenomenological parabolic baseline function $I_{BKG}(\theta) = (-7.8\,\theta^2 + 76)\cdot 10^3$ and a Lorentian curve for the peak. The result yields an enhancement factor value $I_C(0)/I_{BKG}(0) = 1.6$.

For the full width at half maximum of the Lorentian peak we find $\Delta\theta_{EBS} \simeq 10$ deg. This corresponds to a transport mean free path of $l_t = 0.4\,\mu$m, that we obtain by using the standard relation $\Delta\theta_{EBS} = K_{EBS}\frac{\lambda_0}{2\pi l_t}$, with $K_{EBS} = 0.7$. This result is dictated by the value of the pre-factor K_{EBS}, which depends on different aspects of the scattering experiment. The value we use is valid for 3D scattering media and accounts also for long propagation paths contributions [34]. This is a case different from ours, nevertheless in our solar cell the scattering medium lower dimensionality and the presence of absorption tend to respectively reduce and increase the value of the pre-factor, balancing potential deviations. Since a detailed investigation on the EBS effect in our sample is beyond the scope of this work, we consider the calculated value for transport mean free path a satisfactory approximation.

5.6 Light-transport measurement

The results shown so far do not give information on the optical transport of light entering the solar cell. This is an important aspect to evaluate the potential for coherent enhanced absorption (CEA) in our structure is the presence of light transport in the structure. In this section we study the propagation of light trapped inside the solar cell by placing a knife edge immediately in front of the SLM to block half of the incident beam. The resulting light distribution is imaged on the sample surface providing a diffraction limited intensity step.

On the illuminated side, light is scattered into the absorbing layer by the features of the surface morphology, and is guided in the layer stack. This field also diffuses into the dark region, where part of it scatters again on the rough interface. The result is the presence of backscattered light originating also from the non-illuminated area. We study the spatial decay profile of this component of the reflected intensity distribution to obtain information on the light-transport process inside the solar cell.

While illuminating the sample with light polarized along x, i.e. perpendicular to the direction of the knife edge (see Fig. 5.3), we separately detect the two polarization components of the reflected light. We look at a selected area of the image and average over the speckle-like pattern. This area is indicated in Fig. 5.4: it is centred on the beam center, spans the full image in the x direction and 9 μm (100 pixels) in the y direction. The incident intensity in this region is almost independent of y, and by averaging in this direction we obtain the average reflected intensities for both polarizations $\bar{I}_{\parallel}(x)$ and $\bar{I}_{\perp}(x)$,

with that the knife edge positioned at $x = 0$.

Figure 5.9 shows the averaged intensity profiles for the solar cell and the flat silicon sample for both polarization directions $\bar{I}_{\parallel/\perp}(x)$, after normalization to the maximum of the incident intensity $I_{in}(0,0)$. The reflected light originating from the non-illuminated area is the combined result of diffraction effects, light propagation and in and out-of-plan scattering. This *light in the darkness* is most easily observable in the data for orthogonal polarization.

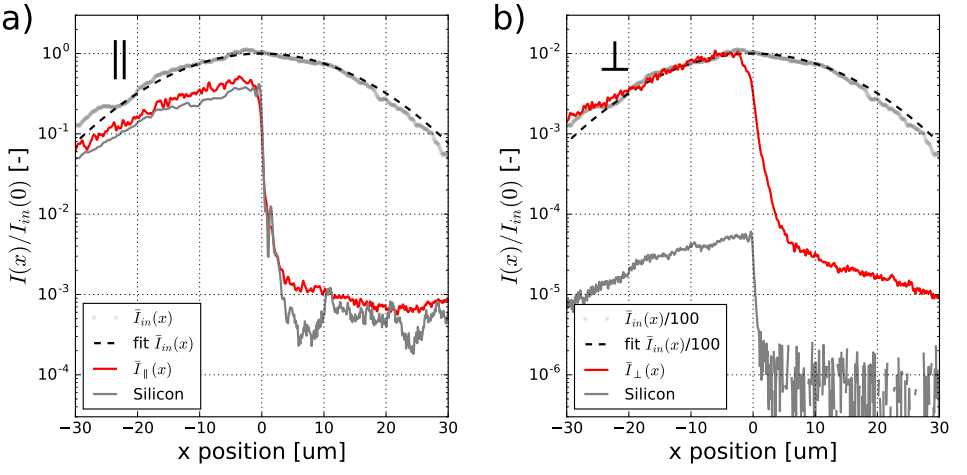

Figure 5.9: Measured average intensities (a) $\bar{I}_{\parallel}(x)$ and (b) $\bar{I}_{\perp}(x)$ normalized to $I_{in}(0,0)$. We show the results for both the solar cell (red) and the flat silicon wafer used as a reference (gray). Both panels also show the incident beam profile in the absence of the knife edge, with the best Gaussian fit, for shape comparison.

5.6.1 Effects of diffraction (reference sample)

As a first step, we study the effect of diffraction. For simplicity, we consider a source in the shape of a half-plane homogeneous illumination positioned at the SLM plane and aligned with the knife edge. The source is described by the field $E_{in}(x) = E_0\,(\frac{1}{2} + \frac{1}{2}\,sign(x))$. The inclusion of the effects of the limited numerical aperture of our optical system yields the following expression for the field incident on the solar cell:

$$E_{out}(x) = \frac{1}{2\pi}\int_{-k_M}^{k_M} e^{ikx}\int_{-\infty}^{\infty} E_{in}(x)\,e^{-ikx}dxdk = E_0\left(\frac{1}{2} + \frac{Si(x\,k_{max})}{\pi}\right) \quad (5.3)$$

with $k_M = 2\pi/\lambda_0$ NA and $Si(y)$ the *sine integral* function defined as $Si(y) = \int_0^y \frac{\sin(t)}{t}dt$.

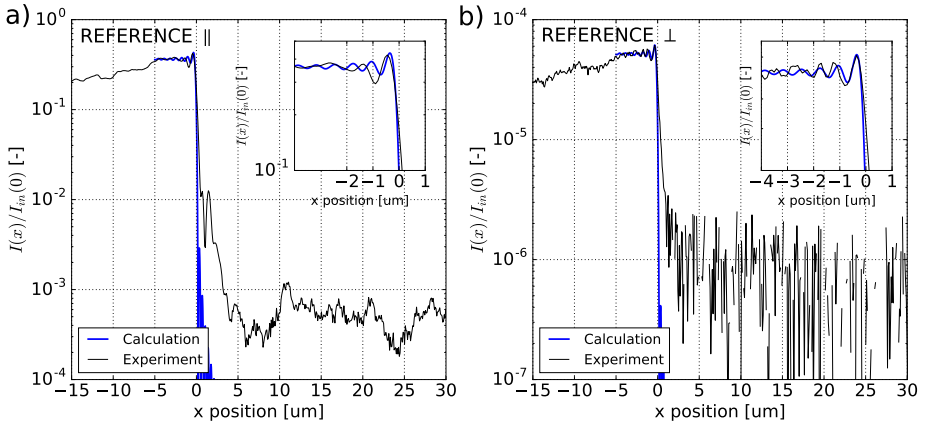

Figure 5.10: Detail of the reflected intensity curves in Fig. 5.9 for (a) parallel and (b) orthogonal polarization for the flat silicon (black line) compared to the model for the diffraction limited image of a half-plane illumination in Eq. (5.3) (blue line). The insets show the detail of the region around $x = 0$.

In Fig. 5.10 we show the results of this calculation for $I_k(x) = |E_{out}(x)|^2$ together with our experimental data. With the peak signal amplitude as the only adjustable parameter, the calculated curve approximately yields the steepness of the knife edge reflection for the reference sample. It also reproduces both amplitude and spatial period of the diffraction fringes in the high intensity region, as highlighted in the insets in Fig. 5.10 (b). The nice agreement between experimental data and theory shows that the spatial resolution in our setup is limited by diffraction. The profile $\bar{I}_{\parallel}(x)$ for the reference sample contains a spurious signal for $x \gtrsim 0$ μm. As mentioned previously, we attribute this to light reflected off the microscope objective. This spurious signal is less visible in $\bar{I}_{\perp}(x)$ as it is much weaker there, having a strength comparable to the noise.

5.6.2 Effects of 2D transport (solar cell sample)

The reflected intensity profiles for the knife edge illumination experiment on the solar cell are reported in Fig. 5.11. These show slower intensity decay for $x > 0$ and a rounded feature in the region $-3\,\mu\text{m} < x < 0\,\mu\text{m}$, in place of the sharp kink at $x = 0$ visible for the reference sample. These are both signatures of light diffusion becoming apparent at the light-dark boundary, similarly to the results for the white paint random medium in Ch. 4. The shape of these profiles provide information on the diffusion process.

To model the effect of 2D transport on the reflected intensities $I_{\parallel/\perp}(x)$ we simplify the symmetry of the problem and consider the case of a homo-

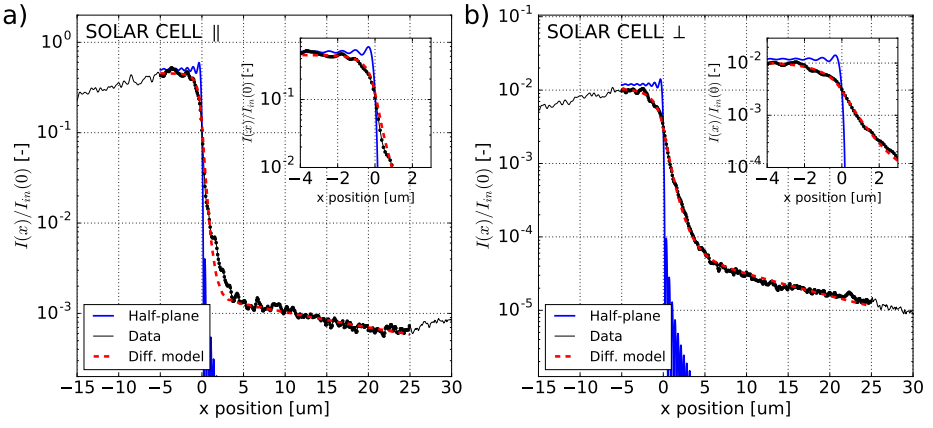

Figure 5.11: Reflected intensity curves for parallel and orthogonal polarization for the solar cell (black lines) with fit curves (dashed red line) from the model (Eq. (5.5)), and the profile for the diffraction limited image of an illuminated half plane in the absence of diffusion (blue line). The insets show the detail of the region around $x = 0$ highlighting the effect of diffusion. The data range used for the fits extends from $x = -5\,\mu$m to $x = 25\,\mu$m.

geneously illuminated half plane; under these conditions the diffusion can be considered a 1D process. For the field diffusion Green's function $G_{1D}(x, x')$ we use the general Ansatz:

$$G_{1D}^{(N)}(x, x') = G_{1D}^{(N)}(x - x') = \sum_{i}^{N} w_i \frac{1}{2\xi_i} e^{-|x-x'|/\xi_i} \tag{5.4}$$

with relative weights $\sum_i^N w_i = 1$, where ξ_i are the field decay lengths of the relevant decay components and $\int_\infty^\infty \frac{1}{2\xi_i} e^{-|x|/\xi_i}\, dx = 1$.

The combined effect of diffraction and field diffusion can be calculated from the convolution of Eqs. (5.3) and (5.4). We use $N = 2$ to allow two separate spatial decay processes and obtain for the intensity profile function:

$$I_{1D}^{(2)}(x) = \left| G_{1D}^{(2)}(x) * E_{out}(x) \right|^2 \tag{5.5}$$

We calculate Eq. (5.5) numerically and fit it to the measured intensity profiles $I_{\parallel/\perp}(x)$ for the solar cell. The results are also shown in Fig. 5.11.

For the orthogonal polarization (panel Fig. 5.11 (b)) this analysis yields a strong fast decay component with $\xi_1^\perp = 1.26 \pm 0.02\,\mu$m and relative weight $w_1^\perp = 0.85 \pm 0.01$, and a slow decay component with $\xi_2^\perp = 25 \pm 2\,\mu$m. For the parallel polarization (panel Fig. 5.11 (a)) the fit yields $\xi_1^\parallel = 0.55 \pm 0.01\,\mu$m

with a relative weight $w_1^{\parallel} = 0.89 \pm 0.01$ and a slowly decaying component with $\xi_2^{\parallel} = 41 \pm 7\,\mu$m.

The features of the reflected intensity profiles for knife edge illumination on the solar cell are nicely captured by the model in Eq. (5.5) and yield well-defined values for $\xi_i^{\parallel/\perp}$ and w_i. For parallel polarization the observed signal contains direct reflections from the microscope objective that are not included in Eq. (5.5). On the contrary, the intensity for orthogonally polarized light $\bar{I}_{\perp}(x)$ originates dominantly from depolarization effects caused by the sample structure, as emerges from the comparison with the reference sample. This makes the orthogonal polarization case more reliable and of particular interest; we hence examine this component closely.

The best-fit curve for $\bar{I}_{\perp}(x)$ shows that two spatial decay rates for 1D field diffusion are sufficient to describe the shape of the experimental data. We attribute the value of $\xi_1^{\perp} = 1.26 \pm 0.02\,\mu$m to the actual spatial decay of the light guided inside the layered structure. This decay is very fast and results from the combination of absorption and in-plane scattering in the Si layer, together with the losses due to light escaping the rough structure. By considering only these three processes, we implicitly assume that light trapped in the slab is equally distributed between modes that couple to either parallel or orthogonal polarization components in the far field. Without this assumption, an additional scattering-mediated exchange of energy between two sets of modes should be considered.

The decay at longer scale with $\xi_2^{\perp} = 25 \pm 2\,\mu$m is more difficult to interpret. We identify two possible mechanisms giving rise to such a feature. The first is the presence of guided modes that experience weak absorption and propagate for longer distances in the structure. The second mechanism is light that propagates at the solar cell surface close to grazing angle and scatters over roughness features towards the objective. We examine in more detail the first hypothesis in Sec. 5.7.

5.6.3 Phase-step method applied to solar cells

An alternative approach for measuring the transport properties of a scattering medium is the phase-step method, explained in Ch. 4. In our setup we implement this method by using the SLM positioned at an image plane of the sample. A set of n holograms is displayed on the SLM, with different values of the phase difference $\Delta\Phi_n$ between the two regions indicated with L and R in the inset in Fig. 5.3. In the regions close to the phase-step, the combination

of transport and interference produces a sinusoidal oscillation of the local intensity as a function of $\Delta\Phi_n$. The amplitude of this oscillation $A_{\parallel,\perp}(x,y)$ is a function of the position over the sample and depends on the optical transport in the sample.

We calculate $A_{\parallel,\perp}(x,y)$ from the same region considered for the knife edge experiment, indicated in Fig. 5.4 (a-b). By averaging $A_{\parallel,\perp}(x,y)$ along y we calculate $A_\perp(x)$, shown in Fig. 5.12, which we rescale by the incident intensity to obtain a relative amplitude oscillation. We don't present the results for the reflection in parallel polarization as these are again affected by the interfacial reflections from the microscope objective.

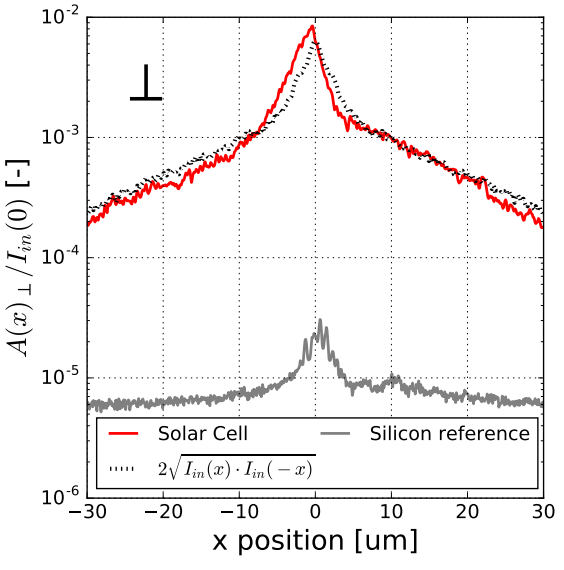

Figure 5.12: Results of the phase-step method applied on the solar cell. The average amplitude of the intensity oscillation $A_\perp(x)$ for the solar cell (red line) is compared with the same quantity measured on the flat Si (light gray). The dashed curve shows the equivalent curve $f(x) = 2\sqrt{\bar{I}_\perp(x)\,\bar{I}_\perp(-x)}$ calculated using the results from the knife experiment.

Figure 5.12 shows that the signal $A_\perp(x)$ is much stronger for the solar cell than for the reference and hence is a reliable signal. The shape of $A_\perp(x)$ provides information on the transport and scattering properties of the solar cell: it shows two main regions for $|x| \lesssim 5\,\mu$m and $|x| \gtrsim 5\,\mu$m, with respectively a faster and slower decay of the function value.

In chapter 4 we noted that the phase-step and knife-edge experiments yield similar information. We highlight this by comparing $A_\perp(x)$ with the equivalent curve obtained from the knife-edge data $f(x) = 2\sqrt{\bar{I}_\perp(x)\,\bar{I}_\perp(-x)}$, to obtain good quantitative agreement (see Fig. 5.12). The only difference between the two cases is the larger amplitude of the phase-step signal as compared to the knife edge measurements.

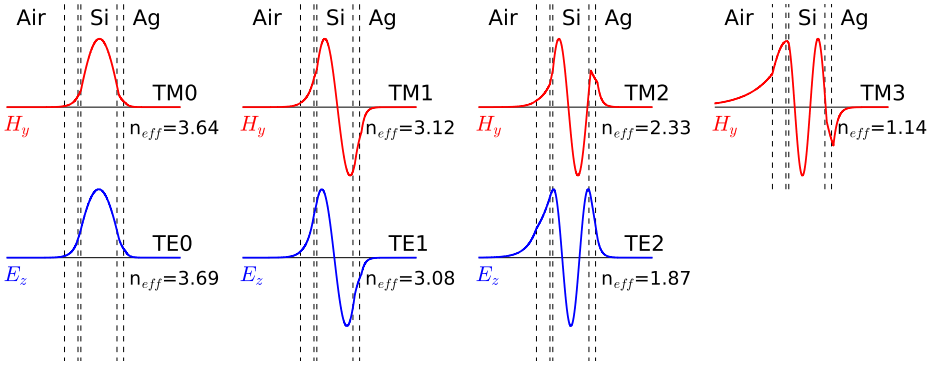

Figure 5.13: Field profiles for (Top) the (in-plane) magnetic field component for the TM guided modes and (Bottom) the (in-plane) electric field component for TE modes supported by the flat layered structure.

5.7 Guided modes in the layered structure

The structure of our solar cell supports guided modes, but their free propagation is affected by roughness-induced scattering. The supported guided modes and their properties can be determined using the *transfer matrices technique*, a standard method in stratified media, considering a smooth layered waveguide in place of our rough structure. This allows to calculate typical propagation lengths of the eigenmodes of the structure in the absence of scattering but in presence of absorption.

Transfer matrices are generally used to model reflection and transmission of plane waves in multilayer structures. These 2×2 matrices relate the amplitudes of forward and backward propagating plane waves components within the different layers of the structure. The overall transfer matrix M^π of the layer stack is obtained, for each polarization $\pi = TM/TE$, by multiplications of the matrices $T^\pi_{i,j}$ and P^π_i describing respectively the refraction at the i-j interface and propagation in the i-th layer.

Here we calculate the transfer matrices for our system $M^\pi(k_\parallel)$ as functions of the in-plane component of the wavevector. For the optical properties of the materials we use the complex valued permittivities $\epsilon = \epsilon' + i\epsilon''$, indicated in Tab. 5.1. Real valued ϵ are considered only for the doped SiO_x layers, which are very thin and hence have little influence. The guided modes supported by a stack correspond to the minima of the matrix element $M^\pi_{1,1}(k_\parallel)$ in the range for $k_\parallel > 2\pi/\lambda_0$ where modes have field evanescent in air. More details on the

method we use are available in Ref. [38]. The field profiles for the allowed modes are shown in Fig. 5.13.

	ϵ_r	thickness [nm]
Air	1.00	-
ITO	3.18+j0.01	75
p-SiO_x-H	7.29	16
i-Si-H	15.07+j0.15	200
n-SiO_x-H	4.84	37
Ag	-18.29+j0.48	300

Table 5.1: Values of the relative permittivity of the materials of the solar cell layers. Values for the thicker layers are obtained from literature for $\lambda = 633$ nm (ITO [35], Si [36], Ag [37]). For the p and n doped regions we use the refractive index for $\lambda = 800$ nm specified by the producer of the sample (TU Delft, Prof. M. Zeman Group): the precise value of these refractive indices is less important due to the very small thickness of the doped layers.

Guided light is mainly absorbed in the Si layer, where most of the field is localized, and partially in the metallic reflector. We can calculate the absorption decay rate in the stack by considering the absorption as a weak perturbation to a non-absorbing system. This approximation is justified when the complex refractive indices $n = n' + in''$ of the absorbing media are such that $n'' \ll n'$, as for the case of Si with $n_{Si}(\lambda = 633\,\mathrm{nm}) = 3.88 + j0.02$.

Given the values for $k_{\|}$ for each of the allowed modes it is possible to also calculate the imaginary part of the effective refractive index $n_{eff} = n'_{eff} + i\, n''_{eff}$, where $n'_{eff} \equiv k_{\|}/k_0$. We use the results from [39] which read:

$$\text{TE modes}: \quad n''_{eff} = \frac{k_0}{2\, n_{eff}} \frac{\int_\infty^\infty \epsilon''_r |E_y|^2\, dz}{\int_\infty^\infty |E_y|^2\, dz} \tag{5.6}$$

$$\text{TM modes}: \quad n''_{eff} = \frac{n_{eff} k_0}{2} \frac{\int_\infty^\infty \epsilon''_r |E_z|^2\, dz}{\int_\infty^\infty \epsilon'_r |E_z|^2\, dz} \tag{5.7}$$

where the expression for the TM modes is an approximation based on the assumption $E_x \ll E_z$ [39].

The results for the effective refractive indices of the allowed guided modes are reported in Table 5.2, where we also calculate the absorption length $L_{abs} = \lambda/(4\pi\, n''_{eff})$. All calculated absorption propagation lengths L_{abs} are larger than the measured diffusion length for the field reported in Sec. 5.6.

	n'_{eff}	n''_{eff}	L_{abs} [μm]
TE0	3.69	0.018	2.7
TE1	3.08	0.015	3.4
TE2	1.87	0.008	6.1
TM0	3.64	0.018	2.8
TM1	3.12	0.008	6.1
TM2	2.33	0.010	5.2
TM3	1.14	0.002	31.8

Table 5.2: Calculated values for the real and imaginary parts of the effective refractive indices n_{eff} of the modes supported by the plane layered structure, together with the absorption propagation lengths L_{abs}.

This is expected as, in the real sample, light transported in the slab is slowed down by scattering in the layer and is subject to losses due to scattering to free space. We can estimate the scattering mean free path l_{sca} using our experimental value for the field decay length for orthogonal polarization $\xi^{\perp}$ and the modelled values for L_{abs} using the relation for the extinction mean free path:

$$l_{ex} = \left(L_{abs}^{-1} + l_{sca}^{-1}\right)^{-1} \tag{5.8}$$

substituting $l_{ex} = \xi_1^{\perp}/2$.

This value accounts for both the scattering within the solar cell as well as the scattering to the outside in the form of backscattered light. This is meant as an estimation and hints to the fact that in our system scattering happens on a scale very similar to absorption.

From table 5.2 we also note that among the modes supported by the slab, the TM3 has a very long absorption length, even longer than the extinction mean free path obtained from the measured slow decay constant for the field $l_{ex} = \xi_2^{\perp}/2 \simeq 12.5\,\mu$m. This supports the hypothesis that the slow intensity decay observed in the knife edge experiment could be caused by a weakly absorbed mode supported by the structure. This mode is bound to also experience less scattering than the other eigenmodes of the structure, but this can only be calculated with a more detailed analysis of 2D scattering.

5.8 Summary

We have studied the scattering of coherent polarized light on a rough solar cell, with the goal to determine the scattering properties of the thin Si film

and the propagation of light trapped in the cell.

We found that the observed light backscattered by our solar cell mostly retains the incident polarization, with only a small fraction (about 2%) of it reflected in the orthogonal polarization. This suggests that the backscattering is dominated by direct reflection from the different layers of the solar cell with a sizeable contribution from the Ag back reflector. Moreover, the reflected signal in both polarization shows correlations with the surface morphology, with the parallel polarization signal coming mostly from the ridges of the roughness profiles.

We studied the backscattered light both as a function of its scattering angle and as a function of the position where it originates on the sample. The spatially resolved measurements with the phase-step method confirmed the result of the knife-edge method.

The depolarization effect is particularly interesting as it provides important information on the scattering process. The angular distribution of the depolarized scattering comprises a four-lobed structure and a azimuthally symmetric (diffuse) component. We attribute the four-lobed component to the effect of the polarization dependence of the Fresnel coefficients upon direct reflection. By modelling the backscattered light from a rough interface with a facets model we explain the four lobes and also a two-lobed feature of the far field in parallel polarization.

The second (diffuse) component of orthogonally polarized backscattering, accounting for about 1% of the total reflection, has possible origin in the field trapped in the solar cells escaping to free space after several scattering events. This component shows a central peak that we attribute to coherent backscattering and that allows us to calculate a value for the transport mean free path of light in the solar cell $l_t \simeq 0.4\,\mu$m.

After studying the angular profile of the scattered light, we investigated its spatial propagation. We illuminated the solar cell with a sharp intensity step, and measured the diffusion into the non-illuminated region of light trapped in the absorbing layer. In this experiment, we again look at the depolarized fraction of the signal, a component not affected by straylight effects. Although transport effects are clearly visible, short propagation distances make it difficult the capture the finest details. We find two different typical extinctions lengths: $l_{ex}^{(1)} = \xi_1^{\perp}/2 = 0.63 \pm 0.01\,\mu$m, and a much longer $l_{ex}^{(2)} = \xi_2^{\perp}/2 = 12 \pm 1\,\mu$m. The value for $l_{ex}^{(1)}t$ is comparable with the value for $l_t \simeq 0.4\,\mu$m calculated from the backscattering cone.

To interpret the observed extinctions lengths we calculate the guided modes supported in a layered structure with plane interfaces instead of roughness, and calculate the absorption lengths in this simplified structure. Despite being very thin, our structure is able to support seven guided modes, including both polarizations. This complicates the analysis, as each mode can experience different scattering mean free path. We find that the most confined modes have an absorption length compatible with the measured shorter extinction length; combining this result with the measurements we calculate a transport mean free path for the most confined modes of $l_t = 0.8\,\mu$m. Additionally, we find that the TM3 mode is weakly absorbed and this might explain the longer extinction length resulting from the measurements.

5.9 Concluding discussion

The experimental investigation we conducted allows to draw some general considerations on the results of our investigation, the possibility of enhancing absorption in our thin-film silicon solar cell, and possible extension of this work.

We were able to measure the extinction mean free path of light in the cell with two methods and to calculate absorption mean free paths, but the number of guided modes involved in optical propagation complicates the interpretation of the experimental parameters. It is probably technologically unrealistic to produce thinner cells supporting fewer eigenmodes, so other approaches need to be followed.

A complete description of the scattering in the solar cell would require two aspects which were not covered in this work: (i) the separation of light scattered within the solar cell structure from the scattering to outside, and (ii) the evaluation of scattering parameters for each of the guided modes separately. Numerical simulations are probably required to achieve this, or (analytic) models that quantify radiative losses on curved two-dimensional waveguides. This would also allow to address the question of how much optical power propagates in each of the guided modes.

The success of wavefront shaping techniques applied to 3D scattering media hinges on their relatively long propagation lengths and low absorption; in our 2D absorbing medium the conditions are very different. Nevertheless, it remains theoretically possible to use wavefront shaping to increase absorption. Follow-up experiments, conducted after this work was completed, indicate

that the light reflected by the solar cell in the orthogonal polarization can be reduced with wavefront shaping techniques by 50%, within the detection cone. This amounts to only 0.5% of the power incident on the cell at 633 nm for our sample and it is probably close to how much more power can be directed to *"absorptive channels"* of the structure, per polarization degrees of freedom.

One natural extension of this work, addressing several of the aspects mentioned above, includes the repetition of the same experiments at longer wavelengths. This would imply a reduction of the absorption in silicon, hence a longer extinction length, and would also reduce the number of eigenmodes in the structure, simplifying the analysis of the experimental data. Longer wavelengths are also of bigger interest in terms of applications: the absorption of silicon decreases for $\lambda > 650\,\text{nm}$, light energy becomes more difficult to harvest.

5.10 Acknowledgments

We are grateful to the group of Electrical Sustainable Energy led by Prof. M. Zeman at the Technical University of Delft, and in particular to Fai Tong Si, for the production, electronic and structural characterization of the sample we used, and to him and Dr. Olindo Isabella for their knowledge and insight in solar cell devices and help in scientific discussion. We also thank the Complex Photonics group of Twente University, and in particular to prof. Willem Vos and Dr. Oluwafemi Ojambati, for scientific discussions.

5.A Depolarization for specular reflections

Reflection from a flat surface can change the polarization state of light as a consequence of the polarization dependence of Fresnel coefficients. This doesn't only happen when the incident light is in the form of a strongly focused spot, as reported in [40], but also when a collimated beam illuminates a tilted surface. We investigate this effect to evaluate the role it can play in the depolarization properties of our solar cell.

We consider a flat surface with its normal tilted by the incidence angle angle θ_{in} with respect to the propagation direction of the incoming light and with azimuthal orientation ϕ. The electric field of the incident light is oriented along the direction $\phi = 0$. For $\phi \neq n\pi/2$ the field incident on the interface is a combination of p and s polarization:

$$E_{in}^{(p)} = E_0 \cos(\phi), \quad E_{in}^{(s)} = E_0 \sin(\phi) \tag{5.9}$$

with E_0 the amplitude of the incident field. After reflection and projection to the far field, one obtains the amplitude of the field reflected for polarization both parallel and orthogonal to the incident one as a function of the reflection angles θ and ϕ:

$$\frac{E_{r,\parallel}(\theta,\phi)}{E_0} = \frac{1}{2}(r_s + r_p) + \frac{1}{2}(r_p - r_s)\cos(2\phi) \tag{5.10}$$

$$\frac{E_{r,\perp}(\theta,\phi)}{E_0} = \frac{1}{2}(r_p - r_s)\sin(2\phi) \tag{5.11}$$

where $r_{s/p} = r_{s/p}(\theta_{in})$ are the Fresnel amplitude reflection coefficients, functions of the incidence angle, with $\theta = 2\,\theta_{in}$ the polar angle for the reflected light collection. We write the associated normalized intensities as:

$$I_\perp(\theta,\phi)/I_0 = a_\perp(\theta)\,\sin^2(2\phi) \tag{5.12}$$

$$I_\parallel(\theta,\phi)/I_0 = a_\parallel(\theta)\,\cos(2\phi) + c_\parallel(\theta) + \frac{a_\parallel^2(\theta)}{4\,c_\parallel(\theta)}\cos^2(2\phi) \tag{5.13}$$

with $I_0 = |E_0|^2$ and $a_\parallel(\theta) = \frac{1}{4}(r_p^2 + r_s^2)$, $c_\parallel(\theta) = \frac{1}{4}(r_p + r_s)^2$, and $a_\perp(\theta) = \frac{1}{4}(r_p - r_s)^2$.

We use an air-Si interface as case study to evaluate the depolarization effect introduced by Fresnel reflection at a tilted interface. In Fig. 5.14 we

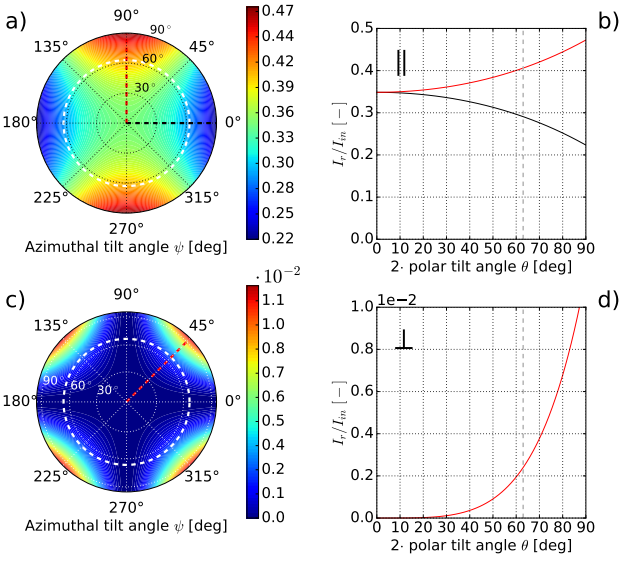

Figure 5.14: Angle dependent reflectivity for a flat surface of Si in air calculated from the models in Eqs. (5.10) and (5.11). (a,c) Reflectivity for (a) parallel and orthogonal (c) polarization $R_{\parallel/\perp}(\theta, \phi)$; (b,d) Values of $R_{\parallel/\perp}(\theta, \phi)$ at relevant azimuthal angles: for parallel polarization (b) for $\phi = 0°$ (black) and $\phi = 90°$ (red) as indicated by dashed lines in (a), and for orthogonal polarization (d) in the direction set by the lobes position $\phi = 45°$. The white dashed lines in (a) and (c) indicate the edge of the acceptance angle in our experiment.

show the calculated $R_{\parallel/\perp}(\theta, \phi) = I_{\parallel/\perp}(\theta, \phi)/I_0$ for a flat Si interface in air. The reflected intensity for parallel polarization shows two maxima and two minima as function of the azimuthal tilt. Most important, the case for orthogonal polarization yields four maxima positioned at tilt angles $\psi = (n + \pi/2)/2$.

Next, we consider the reflection from a rough surface. We interpret the structured interface as an ensemble of flat facets approximating the surface profile [41]. This ray-optics approximation neglects diffraction and interference effects, but could still describe the reflection properties of interfaces with roughness with scale $l_c > \lambda$ and $\sigma_{rms} < \lambda$. To estimate the average far fields expected for a specific interface profile we weight $R_{\parallel/\perp}(\theta, \phi)$ with the probability distributions for the tilt angles $P(\theta_{in}, \phi)$. We obtain the ensemble-averaged far field pattern for reflection:

$$\tilde{I}_{\parallel/\perp}(\theta, \phi) = P(\theta/2, \phi)\, R_{\parallel,\perp}(\theta, \phi) \tag{5.14}$$

The final far field intensity functions have the same form as in Eqs. (5.12-5.13) with the only substitution of the lowercase coefficients with the uppercase version $A_{\parallel}(\theta) = P(\theta/2, \phi)\, a_{\parallel}(\theta)$, $C_{\parallel}(\theta) = P(\theta/2, \phi)\, c_{\parallel}(\theta)$, and $A_{\perp}(\theta) = P(\theta/2, \phi)\, a_{\perp}(\theta)$.

For our sample we calculate $P(\theta_{in}, \phi)$ from the AFM profile after low-pass filtering of the spatial Fourier components of the topology, to remove features smaller than $0.1\,\mu$m (see Fig. 5.2 for a typical AFM profile of a portion of the sample). Since we find no dependence in ϕ, in Fig. 5.15 we show only $P(\theta_{in}) = 2\pi\, sin(\theta_{in})\, P(\theta_{in}, \phi)$.

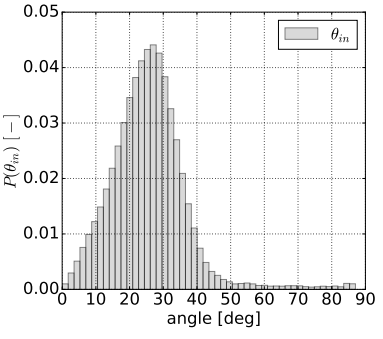

Figure 5.15: Probability density of the polar angle for the local surface normal $P(\theta_{in})$ calculated with respect to the direction of the average plane of the sample.

In Fig. 5.16 we show the far field intensity reflection, calculated from Eq. (5.14) using the function $P(\theta_{in})$ calculated for our sample and applying it to an air-Si interface.

5.B Objective shift to reduce interfacial reflection

To minimize the amount of interfacial reflections from the microscope objective reaching the camera, we shift the objective (100x, $f = 2$ mm) by about $20\,\mu$m along y. This is sufficient to reduce the intensity of the reflection from the objective on the camera by one order of magnitude, as shown from the comparison of the curves in Fig. 5.17. This shift doesn't appear to affect the steepness of the intensity step. However, it does introduce an unwanted reflection close to the intensity step ($0 < x < 2\,\mu$m).

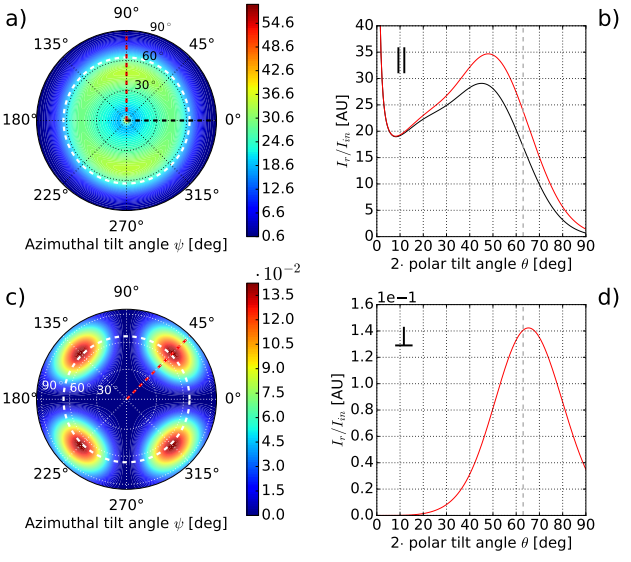

Figure 5.16: Far field reflected intensities from an air-Si interface with morphology similar to our sample, calculated from the models in Eq. (5.14) and based on the AFM data of Fig. 5.2. a) Reflected intensity $\tilde{I}_{\parallel}(\theta, \phi)$. b) Cross sections $\tilde{I}_{\parallel}(\theta)$ for $\phi = 0°$ (black) and $\phi = 90°$ (red), indicated by dashed lines in (a). c) Reflected intensity $\tilde{I}_{\perp}(\theta, \phi)$. d) Cross section $\tilde{I}_{\perp}(\theta)$ for $\phi = 45°$. The white dashed lines in (a) and (c) indicate the edge of the detection angle in our experiment.

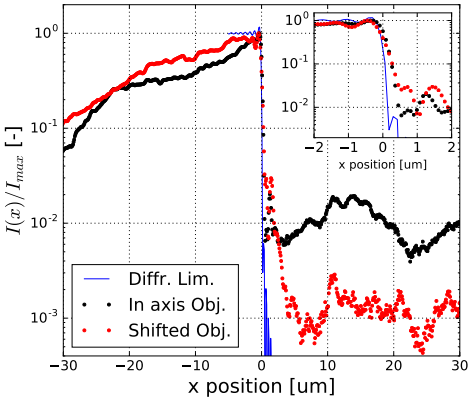

Figure 5.17: Comparison of the curves for the intensity reflected by the reference sample when measured with the microscope objective aligned with the optical axis (black) or shifted by $\Delta y \simeq 20\,\mu\mathrm{m}$ (in black). The light reflected by the objective to the camera is 10 times weaker in the case of a shifted objective. The curve for the diffraction limited image of the knife edge in Eq. (5.3) is also reported for comparison. The inset shows the detail of the curves around $x = 0$.

Bibliography

[1] F. T. Si *et al.*, *Quadruple-junction thin-film silicon-based solar cells with high open-circuit voltage*, Applied Physics Letters **105**, 063902 (2014).

[2] Z. Yu, A. Raman, and S. Fan, *Fundamental limit of nanophotonic light trapping in solar cells*, PNAS **107**, 17491 (2010).

[3] A. Polman and H. A. Atwater, *Photonic design principles for ultrahigh-efficiency photovoltaics*, Nat Mater **11**, 174 (2012).

[4] M. B. Dühring, N. A. Mortensen, and O. Sigmund, *Plasmonic versus dielectric enhancement in thin-film solar cells*, Applied Physics Letters **100**, 211914 (2012).

[5] E. Yablonovitch and G. Cody, *Intensity enhancement in textured optical sheets for solar cells*, IEEE Transactions on Electron Devices **29**, 300 (1982), bibtex: yablonovitch_intensity_1982.

[6] I. Schnitzer *et al.*, *30% external quantum efficiency from surface textured, thin-film light-emitting diodes*, Applied Physics Letters **63**, 2174 (1993).

[7] L. C. Andreani, A. Bozzola, P. Kowalczewski, and M. Liscidini, *Photonic light trapping and electrical transport in thin-film silicon solar cells*, Vol. 135 of *EMRS 2014 Spring Meeting-Advanced materials and characterization techniques for solar cells II*, Solar Energy Materials and Solar Cells **135**, 78 (2015).

[8] M. Zeman *et al.*, *Advanced Light Management Approaches for Thin-Film Silicon Solar Cells*, Vol. 15 of *International Conference on Materials for Advanced Technologies 2011, Symposium O*, Energy Procedia **15**, 189 (2012).

[9] C. van Lare, F. Lenzmann, M. A. Verschuuren, and A. Polman, *Dielectric Scattering Patterns for Efficient Light Trapping in Thin-Film Solar Cells*, Nano Lett. **15**, 4846 (2015).

[10] O. Isabella, J. Krč, and M. Zeman, *Modulated surface textures for enhanced light trapping in thin-film silicon solar cells*, Applied Physics Letters **97**, 101106 (2010).

[11] K. Jäger, M. Fischer, R. A. van Swaaij, and M. Zeman, *Designing optimized nano textures for thin-film silicon solar cells*, Opt. Express **21**, A656 (2013).

[12] M. Burresi *et al.*, *Two-dimensional disorder for broadband, omnidirectional and polarization-insensitive absorption*, Opt. Express, OE **21**, A268 (2013).

[13] C. Rockstuhl *et al.*, *Local versus global absorption in thin-film solar cells with randomly textured surfaces*, Appl. Phys. Lett. **93**, 061105 (2008).

[14] S. Rotter and S. Gigan, *Light fields in complex media: Mesoscopic scattering meets wave control*, Rev. Mod. Phys. **89**, 015005 (2017).

[15] I. M. Vellekoop and A. P. Mosk, *Focusing coherent light through opaque strongly scattering media*, Opt. Lett., OL **32**, 2309 (2007).

[16] I. M. Vellekoop and A. P. Mosk, *Universal Optimal Transmission of Light Through Disordered Materials*, Phys. Rev. Lett. **101**, 120601 (2008).

[17] J. Bertolotti *et al.*, *Non-invasive imaging through opaque scattering layers*, Nature **491**, 232 (2012).

[18] I. M. Vellekoop, E. G. van Putten, A. Lagendijk, and A. P. Mosk, *Demixing light paths inside disordered metamaterials*, Optics Express **16**, 67 (2008).

[19] S. M. Popoff *et al.*, *Measuring the Transmission Matrix in Optics: An Approach to the Study and Control of Light Propagation in Disordered Media*, Phys. Rev. Lett. **104**, 100601 (2010).

[20] Y. D. Chong and A. D. Stone, *Hidden Black: Coherent Enhancement of Absorption in Strongly Scattering Media*, Phys. Rev. Lett. **107**, 163901 (2011).

[21] S. F. Liew *et al.*, *Coherent Control of Photocurrent in a Strongly Scattering Photoelectrochemical System*, ACS Photonics **3**, 449 (2016).

[22] K. Bittkau, R. Carius, and C. Lienau, *Guided optical modes in randomly textured ZnO thin films imaged by near-field scanning optical microscopy*, Phys. Rev. B **76**, 035330 (2007).

[23] K. Bittkau *et al.*, *Nanoscale investigation of light-trapping in a-Si:H solar cell structures with randomly textured interfaces*, phys. stat. sol. (a) **205**, 2766 (2008).

[24] K. Bittkau and T. Beckers, *Near-field study of light scattering at rough interfaces of a-Si:H/μc-Si:H tandem solar cells*, phys. stat. sol. (a) **207**, 661 (2010).

[25] K. Jäger, O. Isabella, R. A. C. M. M. v. Swaaij, and M. Zeman, *Angular resolved scattering measurements of nano-textured substrates in a broad wavelength range*, Meas. Sci. Technol. **22**, 105601 (2011).

[26] M. P. V. Albada and A. Lagendijk, *Observation of Weak Localization of Light in a Random Medium*, Phys. Rev. Lett. **55**, 2692 (1985).

[27] P.-E. Wolf and G. Maret, *Weak Localization and Coherent Backscattering of Photons in Disordered Media*, Phys. Rev. Lett. **55**, 2696 (1985).

[28] E. Akkermans, P. E. Wolf, and R. Maynard, *Coherent Backscattering of Light by Disordered Media: Analysis of the Peak Line Shape*, Phys. Rev. Lett. **56**, 1471 (1986).

[29] A. A. Maradudin and E. R. Méndez, *Enhanced backscattering of light from weakly rough, random metal surfaces*, Appl. Opt., AO **32**, 3335 (1993).

[30] R. E. Luna, E. R. Méndez, J. Q. Lu, and Z.-H. Gu, *Enhanced Backscattering Due to Total Internal Reflection at a Dielectric-air Interface*, Journal of Modern Optics **42**, 257 (1995).

[31] M. P. van Albada, M. B. van der Mark, and A. Lagendijk, *Observation of weak localization of light in a finite slab: Anisotropy effects and light path classification*, Phys. Rev. Lett. **58**, 361 (1987).

[32] M. P. van Albada and A. Lagendijk, *Vector character of light in weak localization: Spatial anisotropy in coherent backscattering from a random medium*, Phys. Rev. B **36**, 2353 (1987).

[33] M. P. v. Albada, M. B. v. d. Mark, and A. Lagendijk, *Polarisation effects in weak localisation of light*, J. Phys. D: Appl. Phys. **21**, S28 (1988).

[34] M. B. van der Mark, M. P. van Albada, and A. Lagendijk, *Light scattering in strongly scattering media: Multiple scattering and weak localization*, Phys. Rev. B **37**, 3575 (1988).

[35] T. A. F. König *et al.*, *Electrically Tunable Plasmonic Behavior of Nanocube-Polymer Nanomaterials Induced by a Redox-Active Electrochromic Polymer*, ACS Nano **8**, 6182 (2014).

[36] D. E. Aspnes and A. A. Studna, *Dielectric functions and optical parameters of Si, Ge, GaP, GaAs, GaSb, InP, InAs, and InSb from 1.5 to 6.0 eV*, Phys. Rev. B **27**, 985 (1983).

[37] P. B. Johnson and R. W. Christy, *Optical Constants of the Noble Metals*, Phys. Rev. B **6**, 4370 (1972).

[38] Y. Pochi, *Optical Waves in Layered Media* (Wiley) (2005).

[39] T. D. Visser, H. Blok, B. Demeulenaere, and D. Lenstra, *Confinement factors and gain in optical amplifiers*, IEEE Journal of Quantum Electronics **33**, 1763 (1997).

[40] L. Novotny, R. D. Grober, and K. Karrai, *Reflected image of a strongly focused spot*, Opt. Lett., OL **26**, 789 (2001).

[41] S.-M. F. Nee *et al.*, *Slope distribution of a rough surface measured by transmission scattering and polarization*, Appl. Opt., AO **39**, 1561 (2000).